Electrical conductivity of the suboceanic upper mantle constrained by satellite-derived tidal magnetic fields: three-dimensional inversion, validation and interpretation

L. Šachl [ID], O. Knopp and J. Velímský

Department of Geophysics, Faculty of Mathematics and Physics, Charles University, V Holešovičkách 2, 180 00, Praha 8, Czech Republic. E-mail:
sachl@karel.troja.mff.cuni.cz

SUMMARY
We present the first 3-D upper-mantle conductivity models obtained by an inversion of the satellite-derived tidally induced magnetic fields (TIMFs). We primarily use the M_2 period, but the potential benefit of the O_1 period is also inspected. The inverse-problem solution is found using the recently developed frequency-domain, spherical harmonic finite-element method based on the adjoint approach. We tested two different TIMF data sets derived from the satellite measurements of the Swarm mission and two different regularizations; the solution is either required to be sufficiently smooth or reasonably close to the *a priori* 3-D conductivity model WINTERC-e Wd-emax. The reconstructed conductivity models are locally compared with the 1-D conductivity profiles from other studies. If we use one of the available TIMF data sets, the smooth reconstructed model gravitates towards Wd-emax and the TIMF-adjusted Wd-emax model is closer to the reference conductivity profiles than the original Wd-emax model. Finally, we use the obtained 3-D conductivity distributions to calculate the corresponding 3-D water distribution in the upper mantle using thermodynamical and compositional models coupled to the electrical-conductivity laboratory measurement of individual mantle constituents.

Key words: Tides and planetary waves; Geomagnetic induction; Inverse theory.

1 INTRODUCTION

The electromagnetic (EM) sounding methods have been used for a long time to infer the electrical conductivity of the Earth's interior. The pioneering works of Chapman & Price (1930) and Lahiri & Price (1939) were published almost 100 yr ago and focused mainly on the theoretical aspects of EM induction (EMI). In the following years, McDonald (1957), Banks (1969), Parker (1971), Banks (1972) and Schultz & Larsen (1987) used continental geomagnetic observatory data to derive the global 1-D conductivity profile of the Earth.

Other authors constructed regional conductivity profiles. Olsen (1999) inspected the lower mantle conductivity beneath Europe using long-period data from the low- and mid-geomagnetic-latitude observatories. Lizarralde *et al.* (1995), Semenov (1998), Utada *et al.* (2003) and Kuvshinov *et al.* (2005) derived the conductivity beneath the North Pacific Ocean by combining data from the coastal geomagnetic observatories and submarine cables. The most comprehensive is the study of Kuvshinov *et al.* (2005), who used data from six observatories and seven cables.

Some regional studies also recovered the lateral conductivity variations besides the average conductivity profile. Utada *et al.* (2009) obtained the 3-D conductivity structure beneath Europe in

the mantle transition zone (MTZ) using data from the 12 European geomagnetic observatories. Fukao *et al.* (2004), Koyama *et al.* (2006) and Shimizu *et al.* (2010) constructed the 3-D MTZ conductivity model beneath the North Pacific Ocean using data from geomagnetic observatories and submarine cables.

A breakthrough in global induction studies has been made by various satellite missions. The key advantage of satellite data is their quasi-global coverage although it takes three months to cover all local times, which creates some trade-off between space and time effects. On the other hand, new challenges have arisen, such as the separation of the inducing and induced fields. Data from the Magsat (Constable & Constable 2004), Ørsted (Civet & Tarits 2013), SAC-C (Kuvshinov & Olsen 2006; Püthe *et al.* 2015), CHAMP (Velímský *et al.* 2006; Martinec & Velímský 2009; Velímský 2010) and Swarm (Civet *et al.* 2015) satellites were used to constrain the global 1-D conductivity structure of the Earth. Kuvshinov & Olsen (2006), Püthe *et al.* (2015) and Grayver *et al.* (2017) combined data from several satellite missions. For example, Püthe *et al.* (2015) used data measured by the Ørsted, CHAMP, SAC-C and Swarm satellites.

The traditional EM sources used to illuminate the upper mantle are the ionospheric (Sq variations) and magnetospheric (Dst variations) electric currents. Satellite measurements have opened the door to the utilization of new EM sources. In particular, the tidally

induced magnetic field (TIMF), first extracted by Tyler *et al.* (2003), has proved to be useful in constraining the upper-mantle conductivity (Grayver *et al.* 2016, 2017).

Recently, the first 3-D mantle conductivity models constructed by inverting a long time-series (several decades) of geomagnetic-observatory data were published by Kelbert *et al.* (2009), Tarits & Mandéa (2010) and Semenov & Kuvshinov (2012). There were notable differences in the reconstructed conductivity structures. The most significant outlier was the model of Tarits & Mandéa (2010) in which the conductivity variations were at least one order of magnitude larger than in the other models. Additionally, in all three cases, the data coverage of the Earth's surface was highly irregular, see fig. 1 in Tarits & Mandéa (2010) or fig. 7 in Semenov & Kuvshinov (2012), and the coverage of suboceanic regions was very poor. The studies of Velímský & Knopp (2021) and Kuvshinov *et al.* (2021) are free of these difficulties. They presented the first 3-D conductivity models of lower mantle constructed from satellite data, specifically Swarm and CryoSat-2 data. Disadvantage of these studies is a relatively low resolution due to the insufficient local-time coverage mentioned above.

In this paper, we follow the lineage of 3-D conductivity studies by further exploiting the usage of satellite data. We present the first attempt to extract information about the 3-D upper-mantle conductivity structure and water content from the satellite-derived TIMFs. The reconstructed models are objectively assessed by comparison with the local conductivity profiles from other studies. The paper aims to demonstrate that the 3-D upper-mantle conductivity can be reconstructed from the satellite-derived TIMFs using our methodology. However, since it is a pioneering work, the presented results might be revisited in the future. In particular, we suggest reexamining the TIMF models since they represent the major source of inaccuracies in the 3-D inverse modelling.

2 METHODOLOGY

2.1 EM inverse problem

We set up the inverse problem according to Šachl *et al.* (2022). The upper-mantle conductivity distribution is numerically discretized using piecewise constant functions on a 3-D curvilinear grid. We fix the conductivity values at subcontinental gridpoints and gridpoints in the Arctic Ocean with colatitudes $\vartheta < 25°$, since the sensitivity of the TIMF inverse problem is poor in this region. We search for the conductivity values in the suboceanic regions. However, since the resolution of the satellite-derived data sets is limited, we search for the conductivity of gridpoint blocks rather than single gridpoints. Thus, the conductivity distribution is given by the model vector $\mathbf{m} \in \mathbb{R}^M$, where M is the number of suboceanic blocks in the inverse problem. The conductivity in the ith block is then equal to $\sigma_i = \sigma_0 10^{m_i}$, where $\sigma_0 = 1\ \mathrm{S\,m^{-1}}$ is used for scaling.

In order to find the conductivity distribution that fits best the satellite-derived TIMF, we minimize the regularized inverse problem,

$$\tilde{\mathbf{m}}(\lambda) = \arg \min_{\mathbf{m} \in \mathbb{R}^M} \left[\chi^2(\mathbf{m}) + \lambda R^2(\mathbf{m}) \right], \quad (1)$$

where $\chi^2(\mathbf{m})$ is the misfit, $R^2(\mathbf{m})$ is the regularization functional and λ is the regularization parameter balancing the data misfit and regularization.

If we consider one tidal constituent at the angular frequency ω, the misfit is defined as a generalized L_2 norm of the differences between the predicted TIMF $\mathbf{B}(\mathbf{m}; r_S, \Omega; \omega)$ and the observed TIMF

$\mathbf{B}^{\mathrm{obs}}(r_S, \Omega; \omega)$ over the sphere S of radius $r_S = a + h$, where $a = 6371.2$ km is the Earth's radius, and $h = 430$ km is the typical altitude of Swarm A+C satellites, $r_S \geq a$,

$$\chi^2(\mathbf{m}) = \frac{1}{2\,S} \int_S M(\Omega) \left| \mathbf{B}(\mathbf{m}; r_S, \Omega; \omega) - \mathbf{B}^{\mathrm{obs}}(r_S, \Omega; \omega) \right|^2 \mathrm{d}S, \quad (2)$$

where $M(\Omega)$ can be an arbitrary function with global support. In our calculations, $M(\Omega)$ is a mask function with values 0 or 1 corresponding to subcontinental and suboceanic blocks.

Here, $\mathbf{B}(\mathbf{m}; r_S, \Omega; \omega)$ is the solution of the motional EMI equation

$$\mathrm{curl}\left[\frac{1}{\sigma(\mathbf{r})} \mathrm{curl}\, \mathbf{B}(\mathbf{r}; \omega) \right] - \mathrm{i}\omega\mu_0 \mathbf{B}(\mathbf{r}; \omega)$$
$$= \mu_0 \mathrm{curl}\left[\mathbf{u}(\mathbf{r}; \omega) \times \mathbf{B}_M(\mathbf{r}) \right]. \quad (3)$$

The external sources are absent, and the interior forcing stems from the interaction of barotropic tidal flows $\mathbf{u}(\mathbf{r}; \omega)$ with the Earth's main magnetic field $\mathbf{B}_M(\mathbf{r})$. More details can be found in Šachl *et al.* (2022) and Velímský *et al.* (2018).

The actual TIMF databases provide internal-field coefficients up to degree j_{maxD} from which the TIMF is calculated,

$$\mathbf{B}^{\mathrm{obs}}(r_S, \Omega; \omega) = \sum_{j=1}^{j_{\mathrm{maxD}}} \sum_{m=-j}^{j} \sum_{\lambda=-1}^{+1} B_{jm}^{(\lambda)}(r; \omega_l) \mathbf{S}_{jm}^{(\lambda)}(\Omega)$$

$$= \sum_{j=1}^{j_{\mathrm{maxD}}} \sum_{m=-j}^{j} G_{jm}^{(\mathrm{i,obs})}(\omega) \left(\frac{a}{r_S} \right)^{j+2}$$

$$\times \left[(j+1)\mathbf{S}_{jm}^{(-1)}(\Omega) - \mathbf{S}_{jm}^{(1)}(\Omega) \right], \quad (4)$$

where $\mathbf{S}_{jm}^{(\lambda)}(\Omega)$ are the complex spherical harmonic (SH) vectors (A1)–(A3) and $G_{jm}^{(\mathrm{i,obs})}(\omega)$ are the SH coefficients of the internal (induced) magnetic field. There are two available satellite-derived TIMF data sets. The MTI data set in versions 601, 701, 801 and 901 (Sabaka *et al.* (2020), released as Swarm Level 2 products by ESA, https://swarm-diss.eo.esa.int/#swarm%2FLevel2longterm%2FMTI) and the GO19 (Grayver & Olsen 2019) data set. We use the GO19 and the latest MTI901 data sets in the inverse modelling. The MTI data sets released earlier are considered only in Section 3.1. The MTI and GO19 data sets are available up to $j_{\mathrm{maxD}} = 18$ and 28, respectively. Both data sets provide the $\mathrm{M_2}$ TIMF, GO19 provides also the $\mathrm{N_2}$ and $\mathrm{O_1}$ TIMFs.

If we insert eq. (4) into eq. (2) and consider that the vectors $\mathbf{S}_{jm}^{(\lambda)}(\Omega)$ are orthogonal to each other, we obtain the equivalent form of the misfit[1]

$$\chi^2(\mathbf{m}) = \sum_{jm} \sum_{j'm'} \left(\frac{a}{r_S} \right)^{j+j'} \left[\overline{G}_{jm}^{(\mathrm{i})}(\mathbf{m}; \omega) - \overline{G}_{jm}^{(\mathrm{i,obs})}(\omega) \right]$$

$$\times W_{jmj'm'} \left[G_{j'm'}^{(\mathrm{i})}(\mathbf{m}; \omega) - G_{j'm'}^{(\mathrm{i,obs})}(\omega) \right], \quad (5)$$

---

[1]Šachl *et al.* (2022) used factor $(a/r_S)^{(j+j')/2}$ in the definition of χ^2, which is technically correct as a weighting but it is inconsistent with eq. (2).

where $W_{jmj'm'}$ is the weighting matrix,

$$W_{jmj'm'} = \frac{1}{8\pi}\left[(j+1)(j'+1)\int_\Omega M(\Omega)\overline{S}_{jm}^{(-1)}(\Omega) \cdot S_{j'm'}^{(-1)}(\Omega)d\Omega \right.$$

$$\left. + \int_\Omega M(\Omega)\overline{S}_{jm}^{(1)}(\Omega) \cdot S_{j'm'}^{(1)}(\Omega)d\Omega\right]. \qquad (6)$$

The weighting matrix is a full matrix if $M(\Omega)$ is a non-trivial function. In a special case when $M(\Omega)$ is a unit function, $M(\Omega) = 1$, the weighting matrix becomes a diagonal matrix due to the orthogonality relation (A4),

$$W_{jmj'm'} = \frac{1}{8\pi}(2j+1)(j+1)\delta_{jj'}\delta_{mm'}. \qquad (7)$$

The weighting matrix (6) satisfies

$$\overline{W}_{j'm'jm} = W_{jmj'm'}, \qquad (8)$$

which guarantees that the misfit is a real-valued function.

If the observed internal-field coefficients have a poor quality at certain SH degree $j = j_p$, for example, due to large measurement errors, it is meaningful to exclude this coefficient from the misfit by using the weighting matrix $\tilde{W}_{jmj'm'}$,

$$\tilde{W}_{jmj'm'} = (1 - \delta_{jj_p})(1 - \delta_{j'j_p})W_{jmj'm'}. \qquad (9)$$

Concerning the regularization, we use two different types. In the first case, we require conductivity distribution to be a smooth field. We thus evaluate the horizontal gradients grad $_\Omega$ of the logarithm of conductivity over the spherical Earth G,

$$R^2(\mathbf{m}) = \frac{1}{a}\int_G \left|\text{grad}\,_\Omega\,\log_{10}\left[\sigma(\mathbf{m};\boldsymbol{r})/\sigma_0\right]\right|^2 dV. \qquad (10)$$

In the second case, we search for the conductive distribution that is close to the *a priori* 3-D conductivity distribution $\sigma_a(\boldsymbol{r})$ by setting

$$R^2(\mathbf{m}) = \int_G \left|\log_{10}\left[\sigma(\mathbf{m};\boldsymbol{r})/\sigma_a(\boldsymbol{r})\right]\right|^2 dV. \qquad (11)$$

2.2 Numerical modelling of TIMFs

2.2.1 Initial conductivity model

We use a similar setup as in our benchmark study Šachl *et al.* (2022). We represent the initial conductivity model with a sphere with 204 layers. The finest resolution is used in the lithosphere and the oceans; our model has 141 layers in the upper 21 km. This is unusual in global EMI studies since the common practice is representing the oceans with only one layer. We agree that the TIMF inaccuracies caused by the one-layer approximation are minor (Velímský *et al.* 2018). However, since the impact of 3-D upper-mantle conductivity is also subtle, as discussed in Section 3.1, we model the 3-D nature of the oceans as precisely as possible. Deeper into the Earth's interior, we use 20 layers in the upper mantle down to 403 km depth, 16 layers in the transition zone and 24 layers in the lower mantle from 676 km down to the core–mantle boundary at a depth of 2876 km. The remaining three layers discretize the Earth's core.

In the oceans, we use the 3-D conductivity distribution of Tyler *et al.* (2017). We neglect the temporal variations of ocean conductivity since we use the annual mean values. The ocean floor is modelled with realistic TPXO9 bathymetry. The conductivity of marine sediments is set according to Grayver (2021). The conductivity of continental sediments is equal to $0.5\,\text{S m}^{-1}$ according to Everett

et al. (2003). A conductivity of $3.48 \times 10^{-4}\,\text{S m}^{-1}$ is assigned to igneous rocks in the crust (Grayver *et al.* 2017).

The initial upper-mantle conductivity is set up according to the Wd-emax model. Wd-emax is a high-conductivity end-member of the WINTERC-e model (Martinec *et al.* 2021) that takes into account water and hydrous melt in the upper mantle. The important feature of WINTERC-e is that it is constructed on the basis of the WINTERC-G model, which has no link to electromagnetism (Fullea *et al.* 2021). By inverting various non-EM geophysical data (seismic waveform tomography, global satellite gravity, surface elevation and heat flow data), WINTERC-G predicts thermal and compositional fields that are combined with the laboratory measurements of the conductivity of upper-mantle minerals and melt to construct the WINTERC-e model.

We use two different initial conductivity distributions in our calculations. The choice depends on the regularization used. In the calculations that are regularized by the horizontal smoothing of conductivity, the initial upper-mantle conductivity is purely 1-D. It is set up according to the Wd-emax1D model, the globally averaged version of the Wd-emax model. In the calculations that are regularized by the distance from the *a priori* conductivity model, both initial and *a priori* upper-mantle conductivity distributions are 3-D in depth range 83-403 km and 1-D in the shallower parts of the upper mantle according to the Wd-emax and Wd-emax1D models, respectively. We set the minimum allowed upper-mantle conductivity in both cases to $10^{-4}\,\text{S m}^{-1}$. The truncation is necessary to avoid the numerical instabilities of the forward solver, but it affects only the shallowest parts of the upper mantle.

We use the 1-D conductivity profile of Grayver *et al.* (2017) in the transition zone and lower mantle and a constant conductivity of $2 \times 10^5\,\text{S m}^{-1}$ (Velímský 2013) in the Earth's core. A more complex model of deep-Earth conductivity is unnecessary since tidal signals do not penetrate to these depths.

2.2.2 Motional forcing

The Lorentz force $\boldsymbol{u}(\boldsymbol{r};\omega) \times \boldsymbol{B}_M(\boldsymbol{r})$ on the right-hand side of the EMI eq. (3) represents the motional forcing dependent on the ocean-flow velocity $\boldsymbol{u}(\boldsymbol{r};\omega)$ and the main magnetic field $\boldsymbol{B}_M(\boldsymbol{r})$. We use tidal velocities predicted by the TPXO9 model (Egbert & Erofeeva 2002, updated), a state-of-the-art hydrodynamic tidal model constrained by satellite altimetry assimilation. In particular, TPXO9 provides the 2-D vertically integrated barotropic velocities, which we scale by local bathymetry to obtain velocities. Note that although the tidal velocity is constant throughout the water column, the motional forcing is 3-D due to the presence of bathymetry that we capture using the fine vertical discretization of the near-surface regions and the 3-D ocean conductivity, see Section 2.2.1. The main magnetic field is given by the International Geomagnetic Reference Field IGRF-13(2015.0) (Alken *et al.* 2021) in the geodetic coordinates up to SH degree 13. The main magnetic field is thus constant in time but 3-D in space since its vertical variations are considered.

2.2.3 ElmgFD solver and the numerical resolution

We use the OpenMP-parallelized EMI solver ElmgFD (Velímský *et al.* 2018) to compute the forward and adjoint fields in the inverse problem. ElmgFD is based on the weak formulation of the EMI equation. It uses the complex vector SH functions in angular coordinates and piecewise-linear 1-D finite elements in the radial coordinate to discretize the governing equations numerically. The

Table 1. Names and locations of the test sites and the authors of the corresponding conductivity profiles used in the presented validation study.

Site	Longitude	Latitude	Author
A	157° E	40° N	Baba *et al.* (2017b)
B	163.5° E	31° N	Baba *et al.* (2017b)
ZHA	165° W	41° N	Zhang *et al.* (2019)
PHS	See the text	See the text	Baba *et al.* (2010)
SAR	145° W	9° N	Sarafian *et al.* (2015)
PAC	147° E	27° N	Baba *et al.* (2017b)
TDC	12.315° W	37.067° S	Baba *et al.* (2017a)

corresponding system of linear equations is solved iteratively using the BiCGStab(2) method (Sleijpen & Fokkema 1993).

The numerical grid is regular in the longitudinal direction and irregular in the latitudinal direction, where the roots of the Legendre polynomial give the gridpoint positions. The grid is irregular in the radial direction, but it is regular in the part of the upper mantle where we search for conductivity values. In this region, the numerical grid has $180 \times 90 \times 20$ points in the longitudinal, latitudinal and radial directions, respectively. It corresponds to approximately 2° in the lateral direction. The resolution in the vertical direction is 20 km. We use the 8° and 10° blocks that contain 4×4 and 5×5 gridpoints in GO19 and MTI901 inversions, respectively, to take into account different j_{maxD}.

We calculate all presented inverse-problem solutions using $j_{max} = 60$, and we apply the data correction of Šachl *et al.* (2022) to account for small-scale ocean flows whose magnetic field does not penetrate into the upper mantle. However, it influences large-scale signals through the galvanic and induction coupling inside the oceans. The data correction is calculated by subtracting $j_{max} = 480$ and 60 TIMF solutions that use 1-D upper-mantle conductivity of Wd-emax1D. We tested that the replacement of Wd-emax1D by the 3-D Wd-emax upper-mantle conductivity has a negligible effect on the data correction.

2.3 Conductivity profiles from other studies

In order to validate the 3-D conductivity models obtained by inversions of TIMF, we compare the local radial conductivity profiles with the conductivity profiles of other authors. We have selected seven 1-D conductivity profiles based on two criteria. First, it needs to be a suboceanic profile, preferably located in the deep ocean. The subcontinental profiles can not be used. However, we accept profiles based on island-observatory measurements provided the island is laterally much smaller than the block used in the inversion. In that case, the impact of the island on the tidal flow and the conductivity of the corresponding oceanic blocks can be neglected. In principle, the profiles from coastal and shelf areas are also acceptable, but our inverse-problem solution might be inaccurate in these regions. Secondly, the upper-mantle conductivity profiles are required. The studies illuminating the lower mantle using periods of a few weeks or months or focusing on the crust or shallow upper mantle using a period range of $10^0 - 10^3$ s are irrelevant for our purposes.

The 1-D conductivity profiles of Zhang *et al.* (2019), Baba *et al.* (2010, 2017a, b) and Sarafian *et al.* (2015) derived from the seafloor magnetotelluric data pass both selection criteria. The names and positions of the respective test sites are summarized in Table 1 and visualized in the lowest-left panel of Fig. 6. The corresponding profiles (reference profiles hereinafter) are depicted in Fig. 7 (and repeated in Fig. 8) as the grey profiles. The A, B, PHS and TDC

profiles provide conductivity up to 400 km depth, while ZHA, SAR and PAC terminate at 300 km depth.

Since our conductivity models are discretized on a structured grid, the gridpoint positions do not coincide with the test-site positions. In most cases, we use the conductivity profile from the nearest gridpoint. The exceptions are the PHS and SAR test sites in the setup with 8° blocks. The PHS profile represents the average conductivity profile of the Philippine Sea. It is a large area, see fig. 1 in Baba *et al.* (2010), it covers approximately 127° E–145° E zonally and 17° N–31° N meridionally. In the case of 8° blocks, four blocks cover the PHS region; thus, we average the respective four conductivity profiles. The SAR test site is located between two neighbouring gridpoint blocks, so we average the conductivity profiles of the two gridpoint blocks. The 8° blocks are used in GO19 inversions. The Wd-emax conductivity model is also averaged to 8° blocks to make a fair comparison.

In order to stay unbiased, we assess the results using a well-defined valuation metric. We call it the discrepancy number d,

$$d = \frac{|| \log_{10} [\sigma(r)/\sigma_{\text{ref}}(r)] ||_2}{\sqrt{r_2 - r_1}}, \qquad (12)$$

where $||.||_2$ is the L^2 norm on the $\langle r_1, r_2 \rangle$ interval and $\sigma(r)$ and $\sigma_{ref}(r)$ are the inspected and reference conductivity profiles, respectively. We calculate d in the depth range of 200–400 km for the A, B, PHS and TDC profiles and 200–300 km for the ZHA, SAR and PAC profiles, which means that $r_1 = a - 400$ km and $r_2 = a - 200$ km, and $r_1 = a - 300$ km and $r_2 = a - 200$ km, respectively. According to Šachl *et al.* (2022), we expect a good sensitivity of TIMFs to conductivity variations in this depth range. We also consider 200 km sufficient to suppress the effect of local small-scale conductivity anomalies on the reference profiles.

2.4 Water-content estimate using thermochemical modelling

2.4.1 Thermochemical modelling

The thermochemical state of the mantle is retrieved from the WINTERC-G model (Fullea *et al.* 2021). The petrological state is derived from the thermochemical variables using the thermodynamical modelling presented in Connolly (1990, 2005, 2009). The input for the aforementioned petrological modelling is the chemical composition in the CFMAS (CaO, FeO, MgO, Al_2O_3 and SiO_2) model, temperature T, pressure P and the thermochemical database presented in Stixrude & Lithgow-Bertelloni (2005a, b) and Xu *et al.* (2008) describing the thermodynamics of the major dry mantle phases. The output for our purpose are the volume fractions X_i^0 of the major mantle phases, specifically olivine (ol), clinopyroxene (cpx), orthopyroxene (opx), garnet and the C2/c pyroxene.

The thermochemical database does not allow us to reliably compute the amount of the peridotite melt present. To get around this, we introduce the possibility of mantle peridotite melting using the water-dependent parametrization described in Katz *et al.* (2003). The melt volume fraction X_f^0 obtained by this parametrization is added to the phase mix, so that the final volume fractions of the phase mix are

$$X_i = \frac{X_i^0}{\sum_{j=1}^{n-1} X_j^0 + X_f^0}, \qquad (13)$$

where $n - 1$ is the number of present phases excluding the melt.

2.4.2 Mantle mineral electrical conductivity

The conductivity of a mantle mineral can be described as $\sigma \equiv \sigma(T, P, X_{\text{Fe}}, C_w)$, where X_{Fe} is molar fraction iron content and C_w is water content described by weight fraction. The formula can be further decomposed into three terms

$$\sigma = \sigma_i + \sigma_h + \sigma_p \,, \tag{14}$$

where σ_i and σ_h are the water-independent conductivity mechanisms (ionic and polaron hopping) and σ_p is the water-dependent proton conductivity.

The water independent conductivity terms for orthopyroxene and clinopyroxene are the same as the ones used in Fullea *et al.* (2011). For the dry conductivity of garnet, we used the measurement results presented in Dai & Karato (2009). For the water-dependent conductivity terms, we use the same dependencies as in Martinec *et al.* (2021). That is for clinopyroxene and orthopyroxene we use the results presented in Zhao & Yoshino (2016) and Zhang *et al.* (2012), respectively. Furthermore, due to lack of data for C2/c pyroxene, we consider its conductivity dependency to be the same as the one of orthopyroxene. For the conductivity of melt, we apply the formula by Ni *et al.* (2011).

As olivine is the major upper-mantle phase, we consider several electrical conductivity parametrizations. These parametrizations are presented in Gardés *et al.* (2014), Xu *et al.* (2006) and Yoshino *et al.* (2009, 2012). For each of these parametrizations, we computed the water content inversion. Only the results for the first two parametrizations are presented because using the parametrization of Yoshino results in unrealistically high water content for the upper mantle.

Due to the uncertainty of phase mix structure, we consider only the lower and upper Hashin–Shtrikman (HS) bounds for the bulk electrical conductivity. The HS electrical conductivity bounds for the phase mix of n present phases can be computed as

$$\sigma_{\text{HS}}^{\pm} = \left(\sum_{i=1}^{n} \frac{X_i}{\sigma_i + 2\sigma_{\pm}} \right)^{-1} - 2\sigma_{\pm} \,, \tag{15}$$

where σ_{HS}^{+} and σ_{HS}^{-} are the upper and lower HS bound and σ_{+} and σ_{-} are the maximal and minimal conductivities for the present phases, respectively.

2.4.3 Water

The water content of the upper mantle is not accounted for in the thermochemical modelling within the CFMAS model. For our purposes, it is considered to be a free parameter on top of thermodynamical modelling.

The water content is not distributed evenly among the present phases. The bulk water concentration is equal to

$$C_w = \sum_{i=1}^{n} X_i C_w^i \,, \tag{16}$$

where X_i are the phase volume fractions and C_w^i are the corresponding water concentrations.

The distribution of water content between phases is not independent and can be described by water partition coefficients. The water partition coefficient $D_{i/j}$ between two phases i and j is defined as $C_w^i = D_{i/j} C_w^j$. First, we consider the peridotite-melt partition coefficient $D_{\text{per/melt}} = 0.01$ used in Katz *et al.* (2003). Therefore, the

equation for melt water content is

$$C_w = C_w^{\text{melt}} \left(X_{\text{melt}} + D_{\text{per/melt}} X_{\text{per}} \right)$$
$$= C_w^{\text{per}} \left(D_{\text{per/melt}}^{-1} X_{\text{melt}} + X_{\text{per}} \right) \,. \tag{17}$$

To partition the water content of peridotite between olivine, orthopyroxene and clinopyroxene, we employ the results of Demouchy *et al.* (2017). We use the olivine–orthopyroxene water partition coefficient $D_{\text{opx/ol}} = 10.6$ and the olivine–clinopyroxene water partition coefficient $D_{\text{cpx/ol}} = 5.6$. The equation describing the water contents of the present peridotite phases is

$$C_w^{\text{per}} = C_w^{\text{ol}} (X_{\text{ol}} + D_{\text{cpx/ol}} X_{\text{cpx}} + D_{\text{opx/ol}} X_{\text{opx}} + D_{\text{opx/ol}} X_{\text{C2/c}}) \,. \tag{18}$$

We consider the C2/c pyroxene to have the same water partition properties as orthopyroxene, due to the lack of data. Furthermore, following Martinec *et al.* (2021), we set the water content of garnet to zero. Lastly, we neglect any water saturation effects on the water partitioning.

3 RESULTS

3.1 Satellite-derived TIMFs

We start with the inspection of the Lowes–Mauersberger spectra of the MTI and GO19 (see Section 2.1) M_2 TIMFs at the satellite height of 430 km. Fig. 1 shows six power spectra up to SH degree 18 of the five satellite-derived TIMFs and the synthetic TIMF calculated using the 3-D Wd-emax upper-mantle conductivity and the TPXO09 M_2 tidal flow, see Section 2.2. The maximum SH degree is set to $j_{\max} = 480$, which is considered to be a sufficiently fine resolution.

Qualitatively, the shape of all spectral lines in Fig. 1 agrees well, and the spectral peaks match nicely. However, the MTI spectra are significantly more energetic than the GO19 and Wd-emax spectra, except for the spectrum of the latest MTI901 data set. The power gradually decreases from MTI601 to MTI901, but the power reduction in MTI901 is the most dramatic change in the MTI lineage. Consequently, the GO19 and MTI901 spectra match the synthetic Wd-emax spectrum considerably better than the MTI601, MTI701 and MTI801 spectra. An exception is SH degree 1, which differs in the GO19 spectrum from the Wd-emax and MTI spectra. We consider it to indicate that degree 1 is overly strong in GO19. We argue that it could be a remnant of a non-tidal EM field that has not been successfully separated.

We continue with the direct comparison of the GO19 and MTI901 coefficients. We follow Sabaka *et al.* (2020) and calculate normalized coefficient differences in absolute value,

$$S_{jm} = \begin{cases} \left| h_{jm}^{(i,\text{MTI901})} - h_{jm}^{(i,\text{GO19})} \right| / N_j, & \text{for } m < 0 \\ \left| g_{jm}^{(i,\text{MTI901})} - g_{jm}^{(i,\text{GO19})} \right| / N_j, & \text{for } m \geq 0, \end{cases} \tag{19}$$

where $g_{jm}^{(i,\text{obs})}$ and $h_{jm}^{(i,\text{obs})}$ are the Schmidt semi-normalized real Gauss coefficients corresponding to the cosine and sine terms, respectively, and N_j is the normalization factor,

$$N_j = \sqrt{\frac{1}{2j+1} \sum_{m=0}^{j} \left[\left(g_{jm}^{(i,\text{GO19})} \right)^2 + \left(h_{jm}^{(i,\text{GO19})} \right)^2 \right]}, \tag{20}$$

that is, GO19 is the 'reference' model and MTI901 is the 'evaluated' model.

Fig. 2 shows the matrices of $S(j, m)$ differences for the real and imaginary parts of the TIMF up to degree 10. It is striking that many
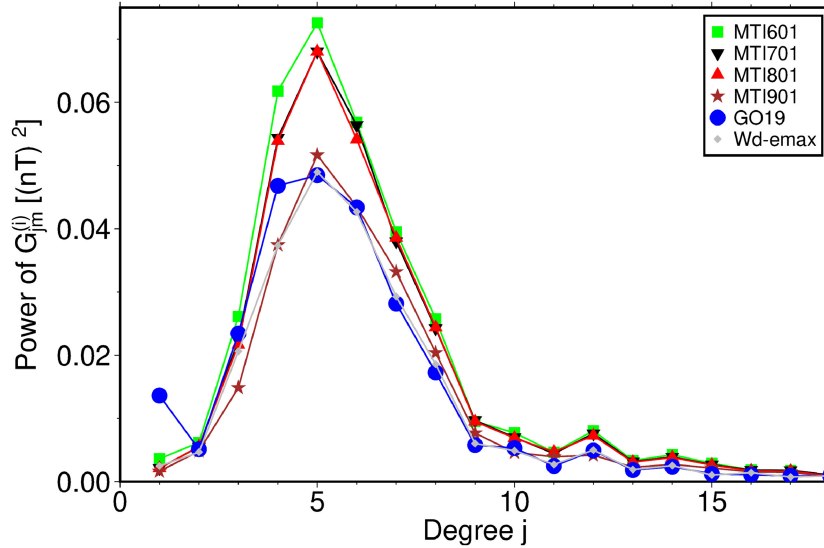
Figure 1. Lowes–Mauersberger spectra of the M_2 TIMFs. The spectra of the satellite-derived MTI and GO19 TIMFs and the spectrum of the synthetic TIMF calculated using the Wd-emax upper-mantle conductivity are shown.
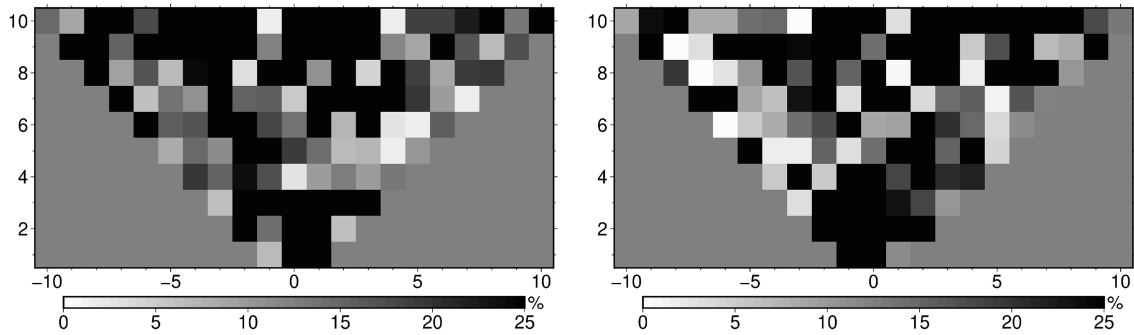
Figure 2. Normalized coefficient differences of real (left-hand panel) and imaginary (right-hand panel) parts of the MTI901 TIMF with respect to the GO19 TIMF in absolute value up to degree 10.

coefficients are significantly different, although specific coefficients are very similar in both data sets. It also means that there does not exist an offset or a multiplication factor that would scale the MTI901 or GO19 coefficients to each other. The level of mismatch between the GO19 and MTI901 coefficients is similar in real and imaginary components. The misfit éq. (5) is thus defined reasonably, and its modification that would consider only real or imaginary parts of the internal coefficients is not justified.

The radial component of the GO19 and MTI TIMFs at 430 km height can be found in the original papers. The synthetic M_2 TIMF synt1D calculated using the 1-D upper-mantle conductivity model Wd-emax1D, which is the globally averaged Wd-emax model, is in good agreement with those figures, see the first column of Fig. 3. The expected imprint of the 3-D upper-mantle conductivity in the TIMF on a satellite height is subtle, see the second column of Fig. 3. It depicts the differences between the synthetic TIMF synt3D calculated using the 3-D Wd-emax upper-mantle conductivity and the synt1D TIMF. The GO19 and MTI901 TIMF differences with respect to the synt1D TIMF are shown in the third and fourth columns of Fig. 3, respectively. It is concerning that the amplitudes of GO19-synt1D and MTI901-synt1D differences are about one order of magnitude larger than the amplitude of synt3D-synt1D differences. It may either suggest that Wd-emax underestimates the upper-mantle conductivity anomalies or that the imprint of 3-D mantle conductivity

is on the edge (or beyond) of the accuracy of the actual state-of-the-art satellite-derived TIMFs. The first option is supported by the fact that the patterns of GO19-synt1D and MTI901-synt1D differences are similar in the Pacific and Indian Oceans. Nonetheless, there are differences between the two data sets, as we can see in the last column of Fig. 3, especially in the Atlantic Ocean, which supports the second hypothesis. We address this issue in the following sections.

### 3.2 3-D TIMF-derived models of mantle conductivity

We tested two regularization types, the horizontal-smoothness regularization (10) and the regularization towards *a priori* conductivity model (11). It is helpful to start with the conductivity models recovered using the horizontal-smoothness regularization since the positions of conductivity anomalies required by data are identified easily.

3.2.1 Horizontal-smoothness regularization

The conductivity models GO19-SM and MTI901-SM recovered from the M_2 TIMF and the model GO19-SM-O1 recovered from the M_2 TIMF and corrected using the O_1 TIMF as explained in Appendix B are depicted in Fig. 4. The recovered models are displayed for the optimal value of the regularization parameter. Theoretically,
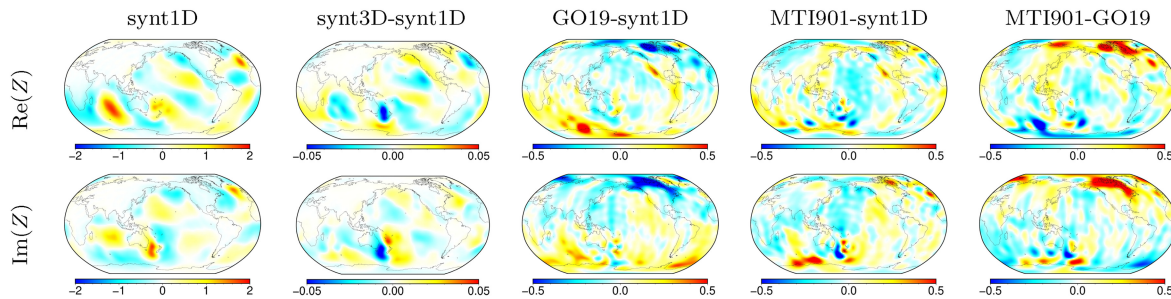
Figure 3. Real (top) and imaginary (bottom) parts of the Z component of the M_2 TIMF [nT] (leftmost column) calculated at the 430 km height using the 1-D upper-mantle conductivity profile Wd-emax1D and the differences [nT] (other columns) with respect to the other M_2 TIMFs.
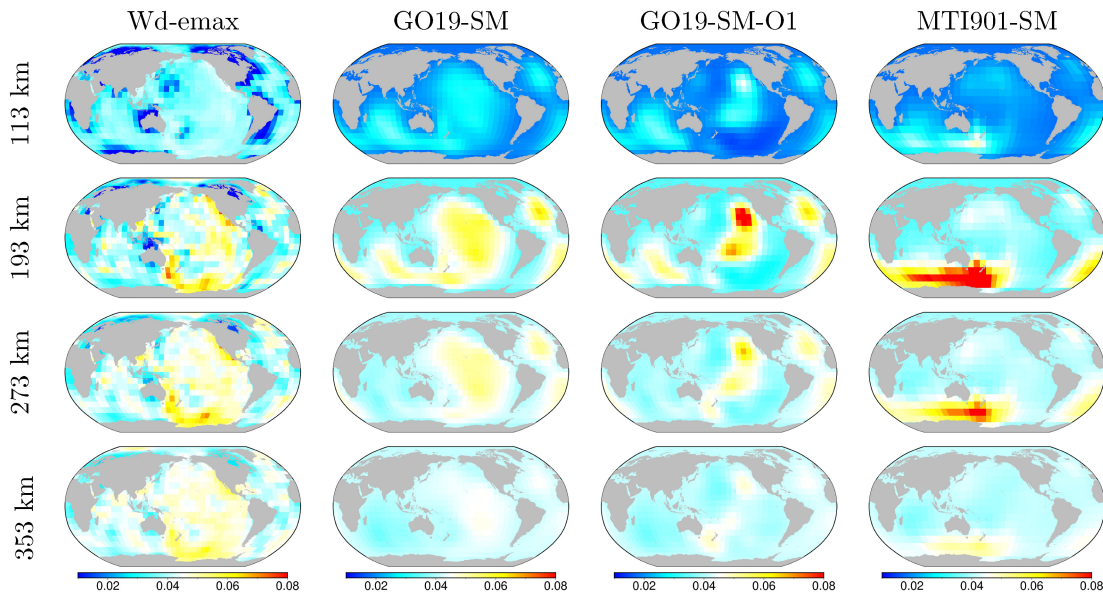
Figure 4. Conductivity models [S m^{-1}] GO19-SM, MTI901-SM and GO19-SM-O1 recovered from the M_2 and M_2+O_1 TIMFs, respectively, using the horizontal-smoothness regularization and the Wd-emax model.

the optimal value corresponds to the maximum inflection point of the L-curve. We thus run a series of regularized inverse problems and choose the optimal value of the regularization parameter by inspecting the L-curve. We identify the inflection point but prefer more regularized solutions since the data quality could be compromised, see Section 3.1.

All SM solutions are more conductive than the Wd-emax1D model in most depths and regions. The largest conductivity anomalies are in the depth range of 183–223 km, see the second row of Fig. 4. The MTI901-SM solution is dominated by the high-conductivity anomaly beneath the Southern Ocean and South Atlantic. The anomaly is centred south of Australia, see the third row of Fig. 4, and it is present in the depth range of 103–363 km, that is, in all inspected depths except for the uppermost and two deepest layers. Less pronounced conductive anomalies are beneath the North Pacific and North Atlantic.

The conductivity anomalies in the GO19-SM solution have different amplitudes, and their locations are shifted. The most evident is that the Pacific and North-Atlantic anomalies are significantly more extensive and conductive. The Southern-Ocean anomaly is reduced; it is localized around Australia but it also extends into the Indian Ocean. The anomaly vanishes below the 243 km depth. The South-Atlantic anomaly is shifted to the north.

The GO19-SM-O1 model is similar to the GO19-SM model, but the Pacific conductivity anomaly is reduced to the banana-shaped feature in the northeast direction from Australia. Additionally, the local maxima are more conductive in GO19-SM-O1.

The Wd-emax model does not enter the inversion with the horizontal-smoothness regularization, and we can thus use this independent piece of information to validate the reconstructed conductivity models. Indeed, since Wd-emax is considered a realistic model of the Earth's interior, the SM models are expected to resemble it closely. Consequently, the TIMFs calculated using the SM models, SM TIMFs for short, are expected to be closer to the Wd-emax TIMF than the Wd-emax1D TIMF. The agreement can be assessed by calculating the corresponding misfits according to eq. (2), where $\boldsymbol{B}$ is the Wd-emax TIMF and $\boldsymbol{B}^{\text{obs}}$ is either the Wd-emax1D, MTI901-SM, GO19-SM or GO19-SM-O1 TIMF. The largest value of misfit is achieved by Wd-emax1D, 4.6×10^{-4} (nT)^2, the misfit decreases slightly to 3.2×10^{-4} (nT)^2 in MTI901-SM and the best misfit value of 8.0×10^{-5} (nT)^2 is achieved by GO19-SM. The misfit in the O$_1$-adjusted model GO19-SM-O1 is higher, equal to 1.91×10^{-4} (nT)^2, which means that the inclusion of the O$_1$ period has worsened rather than improved the M_2-reconstructed conductivity distribution. We argue that it is due to the lower quality and lower cut-off degree of the O$_1$ satellite-derived TIMF with respect

to the better-established M$_2$ TIMF. Because of this result, the O$_1$ TIMF is not considered in the rest of the paper.

As in Section 3.1, we calculate the normalized coefficients differences (19). In this case, the reference data set is Wd-emax TIMF, and the evaluated data sets are Wd-emax1D, GO19-SM and MTI901-SM TIMFs. The respective matrices are depicted in Fig. 5. The GO19-SM differences are lower than Wd-emax1D and MTI901-SM differences, which agrees with the previously calculated misfit values. The MTI901-SM differences are smaller than the Wd-emax1D differences for the lowest degrees, but the discrepancy level is comparable for higher degrees. These results suggest that GO19 data are more suitable for the 3-D upper-mantle inversion of electrical conductivity than MTI901 data.

We wrap up this section with two comments. First, besides MTI901, we also tested the MTI701 and MTI801 TIMFs in the inversion. As indicated by the power spectrum in Fig. 1, the recovered upper-mantle conductivity distributions are far more resistive (not shown) than the GO19 and MTI901 solutions. In fact, MTI701 and MTI801 solutions are more resistive than the Wd-emax1D model in many regions.

Secondly, we do not restrict the vertical conductivity gradients, but since we integrate over the whole Earth in eq. (10), the suboceanic conductivity is connected to the subcontinental conductivity (given by the 1-D model). Modifying eq. (10) and integrating merely over the suboceanic regions where we search for the conductivity values is straightforward. Unfortunately, the recovered model is unrealistically conductive if we use this 'wet' smoothing regularization. Nevertheless, the 'wet' smoothing regularization can be used in the Md60p5j11 synthetic test of Šachl *et al.* (2022). The recovered model is slightly more conductive beneath the coastal regions, but the conductivity values beneath the open ocean and the overall conductivity patterns are not much affected. Considering the first comment, we interpret the difficulties of using the 'wet' smoothing regularization with real data as an indication that a careful treatment of the satellite-derived TIMFs is needed in the 3-D inverse problem.

3.2.2 Regularization towards the Wd-emax conductivity model

The smoothness regularization represents a weak assumption about the upper-mantle conductivity in terms of no *a priori* given positions of conductivity anomalies. However, the level of smoothness of the reconstructed conductivity might be unrealistic. The actual lateral upper-mantle conductivity transitions could be much sharper. We thus propose a different strategy.

Wd-emax is a 3-D model of upper-mantle conductivity, which best agrees with the seismic, gravity and heat-flow data. It is natural to complete the joint inversion by adding EM data. We use Wd-emax as the initial conductivity model and search for conductivity adjustments required by TIMF data. We request the reconstructed conductivity model to be close to Wd-emax, which is achieved by applying the regularization (11) with σ_a given by Wd-emax.

As in Section 3.2.1, the optimal solution of the inverse problem is found by inspecting the L-curve. Additionally, we are also guided by the amount of water in the reconstructed models, see Section 3.4. The recovered conductivity models GO19-AP and MTI901-AP are depicted in Fig. 6. The Wd-emax conductivity model is shown in the left column for comparison. GO19-AP and MTI901-AP solutions are more conductive than Wd-emax in regions where the respective horizontally smoothed counterparts GO19-SM and MTI901-SM display conductive anomalies. Indeed, the regions beneath the Southern Ocean southeast and southwest of Australia and the region

beneath the Atlantic Ocean are more conductive in GO19-AP and MTI901-AP than in Wd-emax. Beneath the North Atlantic, the conductivity is more increased in GO19-AP than in MTI901-AP. Additionally, in GO19-AP, the northeastern part of the North-Pacific region and the part of the Indian-Ocean region above the 200 km depth is more conductive. The conductivity adjustments are larger in the shallower than in the deeper layers. Overall, the adjustments are not extremely large which is in agreement with our concept of conductivity corrections.

3.3 Validation of the recovered 3-D conductivity models

The conductivity profiles of all GO19 and MTI901 solutions are shown in Figs 7 and 8, respectively. In all panels, the reference profiles from other studies are grey, Wd-emax profiles are solid black, Wd-emax1D profiles are dashed black and the solid blue and green profiles correspond to the solutions constrained by the smoothness regularization and the regularization towards Wd-emax, respectively. Note that the post-processed rather than the original profiles are shown. We interpolated (linear interpolation of logarithm of conductivity) each conductivity profile to the common 2-km vertical grid.

The visual inspection reveals a general agreement between our solutions and the reference profiles. In order to be more specific, we calculate the discrepancy number *d* for each conductivity profile. The discrepancy numbers of the Wd-emax1D, Wd-emax and TIMF-derived conductivity models are summarized in Table 2. The conductivity models can be divided into three groups according to the average discrepancy number. The Wd-emax1D model has the largest average discrepancy number. The MTI901-SM and GO19-SM models have approximately 5 and 15 per cent lower average discrepancy numbers, respectively. The Wd-emax, GO19-AP and MTI901-AP models achieve the lowest average discrepancy numbers. To sum it up, Wd-emax outperforms Wd-emax1D, and the TIMF-derived models regularized towards Wd-emax outperform TIMF-derived models with horizontal-smoothness regularization. Both findings are in agreement with our expectations. Indeed, Wd-emax is expected to be a more realistic conductivity model than Wd-emax1D since it contains lateral conductivity variations. Similarly, the AP models combine EM data with other geophysical data; thus, the AP models are expected to be closer to the realistic mantle conductivity than the SM models, which are based purely on EM data.

The GO19-AP model achieves the overall best match with the reference profiles. However, the decrease in the average discrepancy number with respect to Wd-emax is small and it could be considered insignificant. In fact, the discrepancy numbers of A, B and SAR test sites decreased, but the discrepancy numbers of PHS, PAC, ZHA (slightly) and TDC (slightly) sites increased.

It is fair to mention the weak points of the presented validation study. The primary issue is that the coverage of the Global Ocean by the test sites is very irregular. Except for TDC, all test sites are located in the North Pacific. Profiles from the North Atlantic, South Pacific and Indian Oceans would be valuable. A more uniform coverage in the North Pacific would also be useful.

The related problem is that more open-ocean profiles are needed. Considering the 8° and 10° lateral resolution of conductivity models recovered from GO19 and MTI901 TIMFs, respectively, the test sites A, PAC and PHS are not sufficiently far from the coast.

Finally, we might consider discarding the TDC site. It has the largest discrepancy numbers among all test sites, which might be
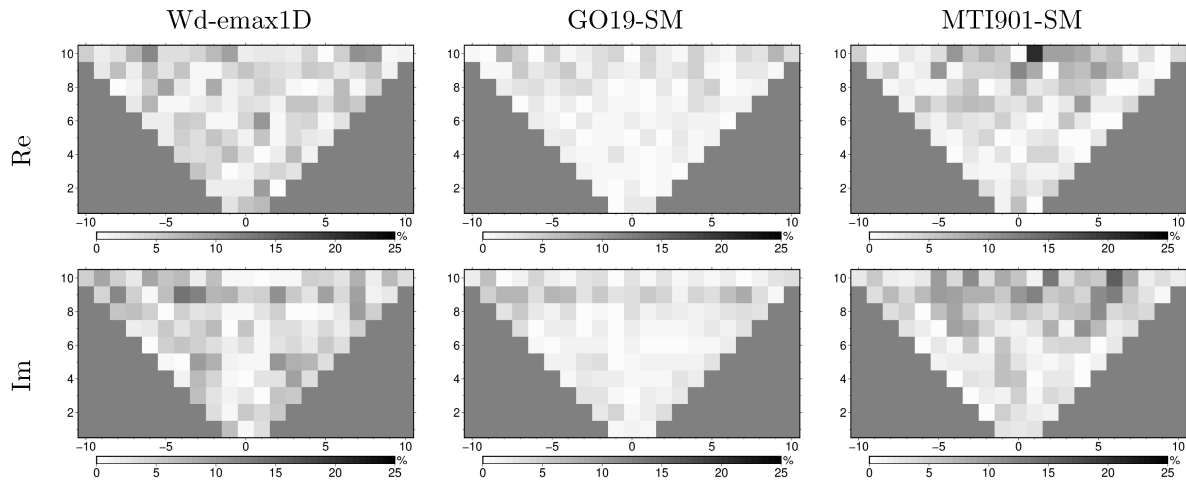
Figure 5. Normalized coefficient differences of real (upper row) and imaginary (lower row) parts of the Wd-emax1D, GO19-SM and MTI901-SM TIMFs with respect to the Wd-emax TIMF in absolute value up to degree 10.
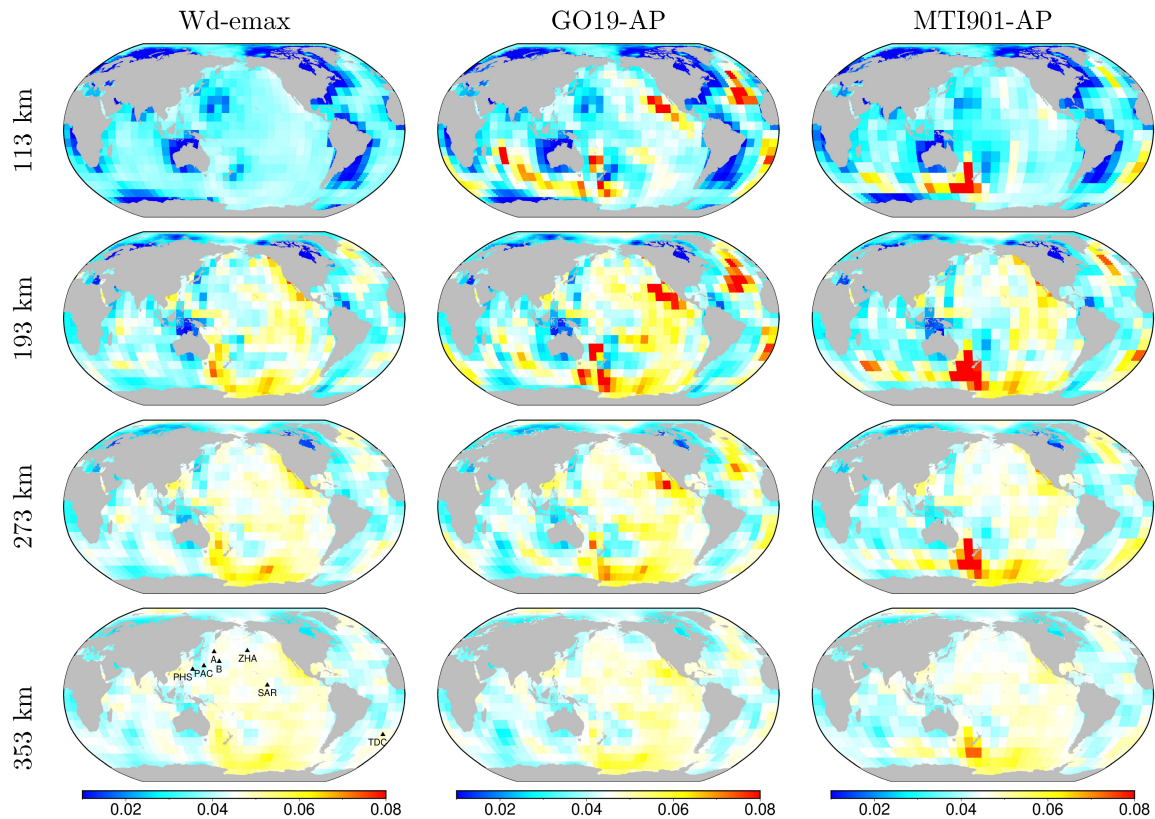

Figure 6. Conductivity models $[\mathrm{S\,m^{-1}}]$ GO19-AP and MTI901-AP recovered from the M_2 TIMFs using the regularization towards Wd-emax (left-hand column).

due to stronger local effects as the seafloor was significantly shallower, approximately 3 km at TDC versus 5 km at other test sites. The problem with the reference conductivity profile is that it decreases from the depth of 140 to 245 km, but then it increases, reaching 0.13 $\mathrm{S\,m^{-1}}$ in the 400 km depth. The conductivity decrease is present in the GO19-SM and MTI901-SM models, but none of our models shows the steep conductivity increase beneath the 245 km depth, see the TDC panels in Figs 7 and 8. The olivine model dissolving 100 ppm water also predicts lower values, see

fig. 8 in Baba *et al.* (2017a). We thus argue that the conductivity increase in the reference profile might be too large.

3.4 Interpretation of 3-D TIMF-derived mantle conductivity

Using thermochemical modelling described in Section 2.4, we derive a family of conductivity models with water content as a free model parameter. This approach allowed us to interpret the
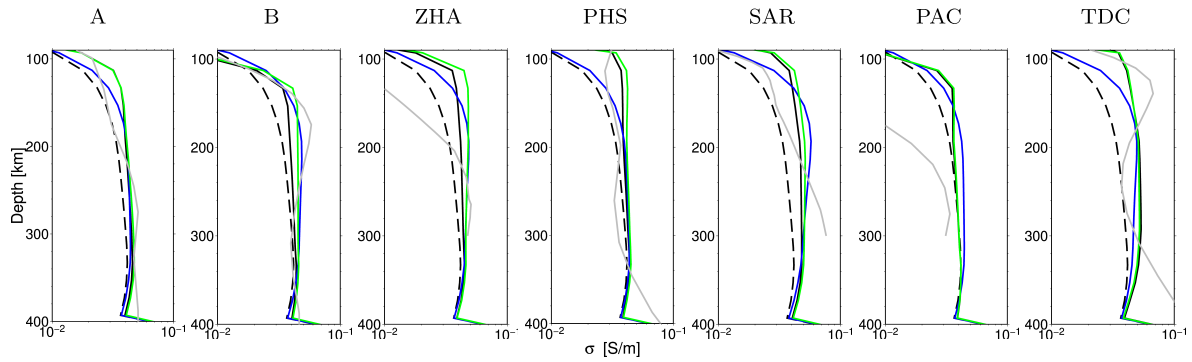
Figure 7. Depth profiles [km] of conductivity [$S\,m^{-1}$] at the selected test sites. Gray, dashed black, black, blue and green profiles correspond to the reference (see Table 1), Wd-emax1D, Wd-emax, GO19-SM and GO19-AP profiles, respectively. The GO19-SM and GO19-SM-O1 profiles are the same for the TDC test site.
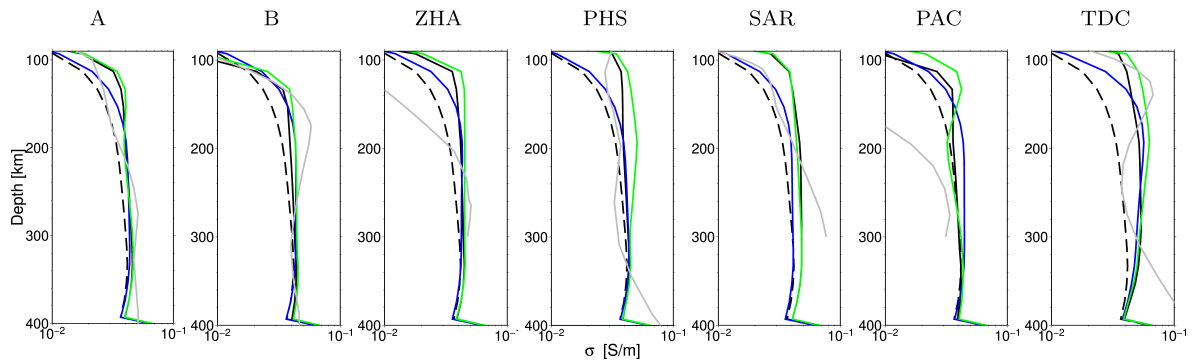
Figure 8. The same as Fig. 7, but blue and green profiles correspond to the MTI901-SM and MTI901-AP profiles, respectively.

Table 2. Discrepancy numbers (12) multiplied by 100 calculated for the Wd-emax1D and Wd-emax conductivity models and the conductivity models recovered from GO19 and MTI901 TIMFs at the selected test sites.

	Wd-emax1D	Wd-emax	MTI901-SM	GO19-SM	MTI901-AP	GO19-AP
A	8,87	4,73	6,41	6,00	4,67	3,82
B	8,16	5,62	4,71	4,58	4,45	4,39
ZHA	9,07	4,69	5,49	5,07	4,32	4,80
PHS	10,07	10,24	11,07	11,18	13,02	10,96
SAR	20,41	11,89	18,06	10,61	12,57	10,13
PAC	13,49	14,58	20,80	20,14	12,12	14,93
TDC	22,28	20,76	21,93	21,69	22,37	20,92
Average	13,19	10,36	12,64	11,32	10,50	9,99

retrieved conductivity models in terms of mantle water content, thereby obtaining lower and upper estimates of water content for the upper and lower Hashin–Shtrikman bounds, respectively. These estimates are constructed pointwise, considering the average temperature and chemical composition within discretization boxes and layers.
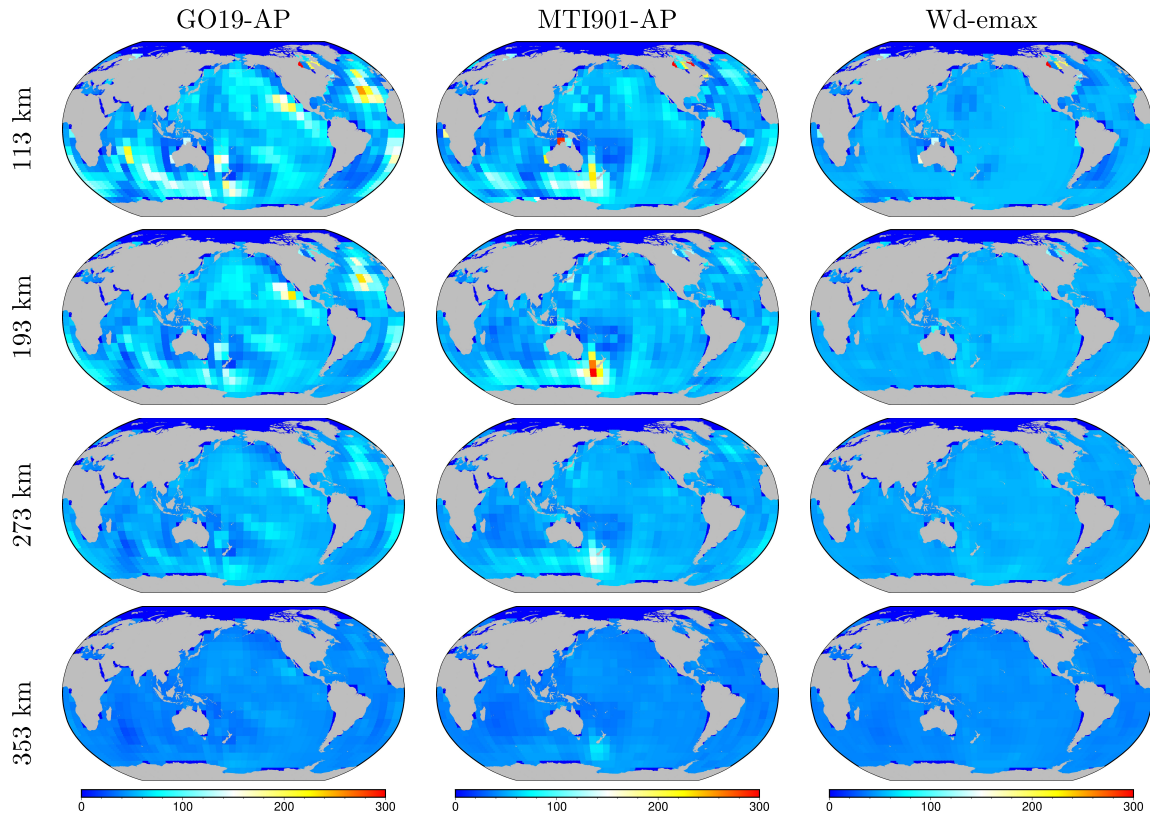
Fig. 9 presents the lower water content estimates for the retrieved GO19-AP and MTI901-AP conductivity models, employing the Xu *et al.* (2006) olivine conductivity. We also included the water content for the Wd-emax model as a reference. Fig. 10 displays a depth profile of a suboceanic average for both the lower and upper estimates of water content derived from GO19-AP in both conductivity models.

When compared to previous studies in Ohtani (2019), the mineral conductivity mode employing Gardés *et al.* (2014) shows a much higher mean water content in the suboceanic upper mantle, even for the lower water estimate. In particular, the average suboceanic water content derived from our conductivity models lies in range

of 100–300 ppm, whereas Khan & Shankland (2012) show water content around 100 ppm. Notice that the range between the upper and lower average suboceanic water content estimates widens for the uppermost layers and the lower upper mantle. This can be solely attributed to the nature of HS bounds, which widen with larger differences between present phase electrical conductivities.

The mineral conductivity model employing Xu *et al.* (2006) applied on the GO19-AP and MTI901-AP mantle conductivity models exhibits reasonable mean water content in the upper suboceanic mantle, around 50–100 ppm, but there are some lateral anomalies of high water content.

Using the GO19-AP conductivity model, we can detect high upper-mantle water content around the mid-Atlantic ridge and at the boundary of the Pacific plate with the North American and Cocos plates. The MTI901-AP model detects high upper-mantle water content around the Southern Indian Ridge and the southern boundary of Pacific and Indo-Australian plates. These features disappear when inspecting the lower depths.

Figure 9. Lower water content estimates in weight fraction [ppm] corresponding to the GO19-AP (left), MTI901-AP (centre) and Wd-emax (right) models.
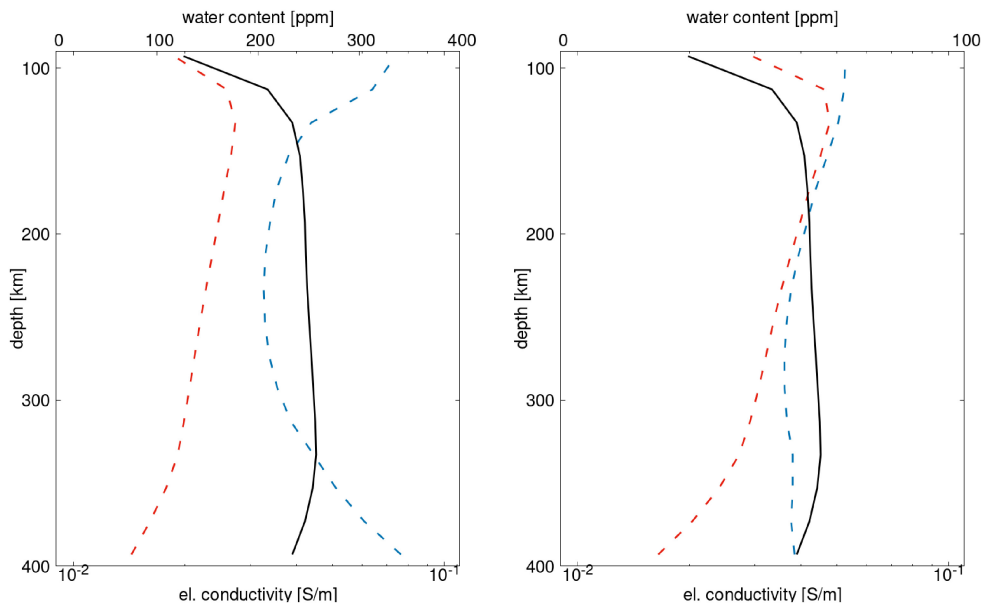
Figure 10. Average suboceanic profile of the lower (red dashed) and upper water (blue dashed) content estimates in weight fraction [ppm] corresponding to the GO19-AP conductivity model (black). Comparison between two rock conductivity model sets, differing in olivine conductivity: Gardés *et al.* (2014) (left) and Xu *et al.* (2006) (right).

There are also extremely high water content anomalies beneath the continents. These can be attributed to the low resolution of our model, which causes the low subcontinental temperatures to affect our conductivity modelling.

The interpretation of electrical conductivity anomaly in terms of water content faces two major challenges. First, there is no standardized method for selecting rock conductivity dependencies, resulting in varied approaches across studies (for a detailed discussion, see Khan & Shankland 2012; Khan 2016, and references therein).

Secondly, the thermochemical modelling of the upper mantle in the presence of partial melt and water is not carried out in a truly self-consistent way. We follow the approach of WINTERC-e (Martinec *et al.* 2021). The thermochemical modelling is carried out only for dry mantle phases. The partial melt, water and its partitioning into all the phases are computed *a posteriori*.

4 CONCLUSIONS

This paper complements the studies of Kelbert *et al.* (2009), Tarits & Mandéa (2010), Semenov & Kuvshinov (2012) and Velímský & Knopp (2021) in the search for the 3-D conductivity structure of the Earth's interior. We restrict ourselves to the suboceanic upper mantle and use the TIMF, which is sensitive to the upper-mantle conductivity. Our main conclusions can be summarized as follows:

• Conductivity models GO19-SM and MTI901-SM reconstructed from the GO19 (Grayver & Olsen 2019) and MTI901 (Sabaka *et al.* 2020) TIMFs, respectively, using the smoothness constraint are more conductive beneath Earth's oceans than the initial WINTERC-e Wd-emax1D model. Both models display conductive anomalies south of Australia beneath the Southern Ocean and beneath the South Atlantic Ocean. In other regions, the location, shape and amplitude of conductivity anomalies in GO19-SM and MTI901-SM do not correspond.

• The GO19-SM and MTI901-SM models agree better with the local conductivity profiles of Zhang *et al.* (2019), Baba *et al.* (2010, 2017a, b) and Sarafian *et al.* (2015) than the initial WINTERC-e Wd-emax1D model but worse than the Wd-emax model. When comparing the SM models, GO19-SM is superior to MTI901-SM since it is closer to the reference conductivity profiles and WD-emax in terms of the corresponding TIMF.

• The GO19-AP model, which uses the M_2 TIMF constraints to adjust the EM-data-free conductivity model WINTERC-e Wd-emax is, on average, closer to the reference profiles than the original Wd-emax model. However, the improvement is small and not very convincing. We recommend repeating the calculations in the future using the next generation TIMF model.

• The conductivity adjustment using the O_1 TIMF does not improve the reconstructed conductivity, although particular improvement has been achieved in the synthetic test. If we consider that the quality of satellite-derived O_1 TIMF is inferior to the M_2 TIMF at the moment, the O_1 TIMF remains promising for future studies.

• Regarding inverse modelling of 3-D upper-mantle conductivity, the TIMF data set MTI901 differs significantly from its predecessor MTI801. The MTI801 power spectrum is much more energetic, and the reconstructed upper-mantle conductivity model MTI801-SM is more resistive than Wd-emax and GO19-SM, which makes it an outlier.

• *A posteriori*, we interpret the recovered suboceanic upper-mantle conductivity models for retrieving the water content using a

set of experimental rock conductivities and thermodynamical modelling of the upper mantle. The amount of water in the suboceanic upper mantle corresponding to the GO19-AP and MTI901-AP conductivity values is realistic. The average water content is in the range of 100–300 ppm. The largest amount of water is stored in the upper parts of the mantle in depths around 140 km. Locally, the water content may reach 500 ppm in regions where the TIMF requires wet conditions.

DATA AVAILABILITY

The results of the inverse modelling will be shared on reasonable request to the corresponding author.

REFERENCES

Alken, P. *et al.*, 2021. International geomagnetic reference field: the thirteenth generation, *Earth Planets Space,* **73**(1), 49, doi:10.1186/s40623-020-01288-x.

Baba, K., Utada, H.,,, Kasaya, T., Shimizu, H. & Tada, N., 2010. Electrical conductivity imaging of the Philippine Sea upper mantle using seafloor magnetotelluric data, *Phys. Earth Planet. Inter.,* **183**(1–2), 44–62.

Baba, K., Chen, J., Sommer, M., Utada, H., Geissler, W. H., Jokat, W. & Jegen, M., 2017a. Marine magnetotellurics imaged no distinct plume beneath the Tristan da Cunha hotspot in the southern Atlantic Ocean, *Tectonophysics,* **716,** 52–63.

Baba, K. *et al.*, 2017b. Electrical conductivity of old oceanic mantle in the northwestern Pacific I: 1-D profiles suggesting differences in thermal structure not predictable from a plate cooling model, *Earth Planets Space,* **69**(1), 1–23.

Banks, R., 1969. Geomagnetic variations and the electrical conductivity of the upper mantle, *Geophys. J. Int.,* **17**(5), 457–487.

Banks, R., 1972. The overall conductivity distribution of the Earth, *J. Geomagn. Geoelec.,* **24**(3), 337–351.

Chapman, S. & Price, A., 1930. The electric and magnetic state of the interior of the Earth, as inferred from terrestrial magnetic variations, *Phil. Trans. R. Soc. A,* **229**(670–680), 427–460.

Civet, F. & Tarits, P., 2013. Analysis of magnetic satellite data to infer the mantle electrical conductivity of telluric planets in the solar system, *Planet. Space Sci.,* **84,** 102–111.

Civet, F., Thébault, E., Verhoeven, O., Langlais, B. & Saturnino, D., 2015. Electrical conductivity of the Earth's mantle from the first Swarm magnetic field measurements, *Geophys. Res. Lett.,* **42**(9), 3338–3346.

Connolly, J., 1990. Multivariable phase diagrams: an algorithm based on generalized thermodynamics., *Am. J. Sci.,* **290**(6), 666–718.

Connolly, J., 2005. Computation of phase equilibria by linear programming: A tool for geodynamic modeling and its application to subduction zone decarbonation, *Earth planet. Sci. Lett.,* **236**(1), 524–541.

Connolly, J., 2009. The geodynamic equation of state: what and how, *Geochem. Geophys. Geosyst.,* **10**(10), doi:10.1029/2009GC002540.

Constable, S. & Constable, C., 2004. Observing geomagnetic induction in magnetic satellite measurements and associated implications for mantle conductivity, *Geochem. Geophys. Geosyst.,* **5**(1), doi:10.1029/2003GC000634.

Dai, L. & Karato, S., 2009. Electrical conductivity of pyrope-rich garnet at high temperature and high pressure, *Phys. Earth Planet. Inter.,* **176**(1), 83–88.

Demouchy, S., Shcheka, S., Denis, C.M.M. & Thoraval, C., 2017. Subsolidus hydrogen partitioning between nominally anhydrous minerals in garnet-bearing peridotite, *Am. Mineral.,* **102**(9), 1822–1831.

Egbert, G.D. & Erofeeva, S.Y., 2002. Efficient inverse modeling of barotropic ocean tides, *J. Atmos. Oceanic Technol.,* **19**(2), 183–204.

Everett, M.E., Constable, S. & Constable, C.G., 2003. Effects of near-surface conductance on global satellite induction responses, *Geophys. J. Int.,* **153**(1), 277–286.

Fukao, Y., Koyama, T., Obayashi, M. & Utada, H., 2004. Trans-Pacific temperature field in the mantle transition region derived from seismic and electromagnetic tomography, *Earth planet. Sci. Lett.,* **217**(3–4), 425–434.

Fullea, J., Muller, M.R. & Jones, A.G., 2011. Electrical conductivity of continental lithospheric mantle from integrated geophysical and petrological modeling: application to the Kaapvaal Craton and Rehoboth Terrane, southern Africa, *J. geophys. Res.: Solid Earth,* **116**(B10), doi:10.1029/2011JB008544.

Fullea, J., Lebedev, S., Martinec, Z. & Celli, N.L., 2021. WINTERC-G: Mapping the upper mantle thermochemical heterogeneity from coupled geophysical-petrological inversion of seismic waveforms, heat flow, surface elevation and gravity satellite data, *Geophys. J. Int.,* **226**(1), 146–191.

Gardés, E., Gaillard, F. & Tarits, P., 2014. Toward a unified hydrous olivine electrical conductivity law, *Geochem. Geophys. Geosyst.,* **15**(12), 4984–5000.

Grayver, A.V., 2021. Global 3-D electrical conductivity model of the world ocean and marine sediments, *Geochem. Geophys. Geosyst.,* **22**(9), e2021GC009950, doi:10.1029/2021GC009950.

Grayver, A.V. & Olsen, N., 2019. The magnetic signatures of the M2, N2, and O1 oceanic tides observed in Swarm and CHAMP satellite magnetic data, *Geophys. Res. Lett.,* **46**(8), 4230–4238.

Grayver, A.V., Schnepf, N.R., Kuvshinov, A.V., Sabaka, T.J., Manoj, C. & Olsen, N., 2016. Satellite tidal magnetic signals constrain oceanic lithosphere-asthenosphere boundary, *Sci. Adv.,* **2**, e1600798, doi:10.1126/sciadv.1600798.

Grayver, A.V., Munch, F.D., Kuvshinov, A.V., Khan, A., Kuvshinov2006, T.J. & Tøffner-Clausen, L., 2017. Joint inversion of satellite-detected tidal and magnetospheric signals constrains electrical conductivity and water content of the upper mantle and transition zone, *Geophys. Res. Lett.,* **44**, 6074–6081.

Katz, R.F., Spiegelman, M. & Langmuir, C.H., 2003. A new parameterization of hydrous mantle melting, *Geochem. Geophys. Geosyst.,* **4**(9), 1073–n/a, doi:10.1029/2002GC000433.

Kelbert, A., Schultz, A. & Egbert, G., 2009. Global electromagnetic induction constraints on transition-zone water content variations, *Nature,* **460**(7258), 1003–1006.

Khan, A., 2016. On Earth's mantle constitution and structure from joint analysis of geophysical and laboratory-based data: an example, *Surv. Geophys.,* **37**(1), 149–189.

Khan, A. & Shankland, T., 2012. A geophysical perspective on mantle water content and melting: Inverting electromagnetic sounding data using laboratory-based electrical conductivity profiles, *Earth planet. Sci. Lett.,* **317–318,** 27–43.

Koyama, T., Shimizu, H., Utada, H., Ichiki, M., Ohtani, E. & Hae, R., 2006. Water content in the mantle transition zone beneath the North Pacific derived from the electrical conductivity anomaly, *Earth's Deep Water Cycle,* **168**, 171–179.

Kuvshinov, A. & Olsen, N., 2006. A global model of mantle conductivity derived from 5 years of CHAMP, Ørsted, and SAC-C magnetic data, *Geophys. Res. Lett.,* **33**(18), doi:10.1029/2006GL027083.

Kuvshinov, A., Utada, H., Avdeev, D. & Koyama, T., 2005. 3-D modelling and analysis of Dst C-responses in the North Pacific Ocean region, revisited, *Geophys. J. Int.,* **160**(2), 505–526.

Kuvshinov, A., Grayver, A., Tøffner-Clausen, L. & Olsen, N., 2021. Probing 3-D electrical conductivity of the mantle using 6 years of Swarm, CryoSat-2 and observatory magnetic data and exploiting matrix Q-responses approach, *Earth Planets Space,* **73**, 67, doi:10.1186/s40623-020-01341-9.

Lahiri, B. & Price, A., 1939. Electromagnetic induction in non-uniform conductors, and the determination of the conductivity of the earth from terrestrial magnetic variations, *Phil. Trans. R. Soc. A,* **237**(784), 509–540.

Lizarralde, D., Chave, A., Hirth, G. & Schultz, A., 1995. Northeastern Pacific mantle conductivity profile from long-period magnetotelluric sounding using Hawaii-to-California submarine cable data, *J. geophys. Res.: Solid Earth,* **100**(B9), 17837–17854.

Martinec, Z. & Velímský, J., 2009. The adjoint sensitivity method of global electromagnetic induction for CHAMP magnetic data, *Geophys. J. Int.,* **179**(3), 1372–1396.

Martinec, Z., Fullea, J., Velímský, J. & Šachl, L., 2021. A new integrated geophysical-petrological global 3-D model of upper-mantle electrical conductivity validated by the Swarm M2 tidal magnetic field, *Geophys. J. Int.,* **226**(2), 742–763.

McDonald, K.L., 1957. Penetration of the geomagnetic secular field through a mantle with variable conductivity, *J. geophys. Res.,* **62**(1), 117–141.

Ni, H., Keppler, H. & Behrens, H., 2011. Electrical conductivity of hydrous basaltic melts; implications for partial melting in the upper mantle, *Contrib. Mineral. Petrol.,* **162**(3), 637–650.

Ohtani, E., 2019. The role of water in Earth's mantle, *Natl. Sci. Rev.,* **7**(1), 224–232.

Olsen, N., 1999. Long-period (30 days–1 year) electromagnetic sounding and the electrical conductivity of the lower mantle beneath Europe, *Geophys. J. Int.,* **138**(1), 179–187.

Parker, R.L., 1971. The inverse problem of electrical conductivity in the mantle, *Geophys. J. Int.,* **22**(2), 121–138.

Püthe, C., Kuvshinov, A., Khan, A. & Olsen, N., 2015. A new model of Earth's radial conductivity structure derived from over 10 yr of satellite and observatory magnetic data, *Geophys. J. Int.,* **203**(3), 1864–1872.

Sabaka, T.J., Tøffner-Clausen, L., Olsen, N. & Finlay, C.C., 2020. CM6: a comprehensive geomagnetic field model derived from both CHAMP and Swarm satellite observations, *Earth Planets Space,* **72**, 80, doi:10.1186/s40623-020-01210-5.

Šachl, L., Velímský, J., Fullea, J. & Martinec, Z., 2022. Inversion of the satellite observations of the tidally induced magnetic field in terms of 3-D upper-mantle electrical conductivity: method and synthetic tests, *Geophys. J. Int.,* **229**(3), 2115–2132.

Sarafian, E., Evans, R.L., Collins, J.A., Elsenbeck, J., Gaetani, G.A., Gaherty, J.B., Hirth, G. & Lizarralde, D., 2015. The electrical structure of the central Pacific upper mantle constrained by the NoMelt experiment, *Geochem. Geophys. Geosyst.,* **16**(4), 1115–1132.

Schultz, A. & Larsen, J., 1987. On the electrical conductivity of the mid-mantle-I. calculation of equivalent scalar magnetotelluric response functions, *Geophys. J. Int.,* **88**(3), 733–761.

Semenov, A. & Kuvshinov, A., 2012. Global 3-D imaging of mantle conductivity based on inversion of observatory C-responses-II. data analysis and results, *Geophys. J. Int.,* **191**(3), 965–992.

Semenov, V.Y., 1998. *Regional Conductivity Structures of the Earth's Mantle,* Polska Akademia Nauk, Instytut Geofizyki.

Shimizu, H., Utada, H., Baba, K., Koyama, T., Obayashi, M. & Fukao, Y., 2010. Three-dimensional imaging of electrical conductivity in the mantle transition zone beneath the North Pacific Ocean by a semi-global induction study, *Phys. Earth planet. Inter.,* **183**(1–2), 252–269.

Sleijpen, G.L.G. & Fokkema, D.R., 1993. Bicgstab(ell) for linear equations involving unsymmetric matrices with complex spectrum, *Electron. Trans. Numer. Anal.,* **1**, 11–32.

Stixrude, L. & Lithgow-Bertelloni, C., 2005a. Mineralogy and elasticity of the oceanic upper mantle: Origin of the low-velocity zone, *J. geophys. Res.: Solid Earth,* **110**(B3), doi:10.1029/2004JB002965.

Stixrude, L. & Lithgow-Bertelloni, C., 2005b. Thermodynamics of mantle minerals – I. Physical properties, *Geophys. J. Int.,* **162**(2), 610–632.

Tarits, P. & Mandéa, M., 2010. The heterogeneous electrical conductivity structure of the lower mantle, *Phys. Earth planet. Inter.,* **183**(1-2), 115–125.

Tyler, R.H., Maus, S. & Luhr, H., 2003. Satellite observations of magnetic fields due to ocean tidal flow, *Science,* **299**(5604), 239–241.

Tyler, R.H., Boyer, T.P., Minami, T., Zweng, M.M. & Reagan, J.R., 2017. Electrical conductivity of the global ocean, *Earth Planets Space,* **69**, 156, doi:10.1186/s40623-017-0739-7.

Utada, H., Koyama, T., Shimizu, H. & Chave, A., 2003. A semi-global reference model for electrical conductivity in the mid-mantle beneath the north Pacific region, *Geophys. Res. Lett.,* **30**(4), doi:10.1029/2002GL016092.

Utada, H., Koyama, T., Obayashi, M. & Fukao, Y., 2009. A joint interpretation of electromagnetic and seismic tomography models suggests the mantle transition zone below Europe is dry, *Earth planet. Sci. Lett.,* **281**(3–4), 249–257.

Varshalovich, D. A., Moskalev, A. N. & Khersonskii, V. K., 1989. *Quantum Theory of Angular Momentum,* World Scientific, Singapore.

Velímský, J., 2010. Electrical conductivity in the lower mantle: Constraints from CHAMP satellite data by time-domain EM induction modelling, *Phys. Earth planet. Inter.,* **180**(3–4), 111–117.

Velímský, J., 2013. Determination of three-dimensional distribution of electrical conductivity in the Earth's mantle from Swarm satellite data: Time-domain approach, *Earth Planets Space,* **65,** 1239–1246.

Velímský, J. & Knopp, O., 2021. Lateral variations of electrical conductivity in the lower mantle constrained by Swarm and CryoSat-2 missions, *Earth Planets Space,* **73**(1), 1–12.

Velímský, J., Martinec, Z. & Everett, M. E., 2006. Electrical conductivity in the Earth's mantle inferred from CHAMP satellite measurements-I. Data processing and 1-D inversion, *Geophys. J. Int.,* **166**(2), 529–542.

Velímský, J., Grayver, A., Kuvshinov, A. & Šachl, L., 2018. On the modelling of M$_2$ tidal magnetic signatures: effects of physical approximation and numerical resolution, *Earth Planets Space,* **70**(1), 70–192.

Xu, W., Lithgow-Bertelloni, C., Stixrude, L. & Ritsema, J., 2008. The effect of bulk composition and temperature on mantle seismic structure, *Earth planet. Sci. Lett.,* **275**(1), 70–79.

Xu, Y.,,,, Wang, D. & Mookherjee, M., 2006. The effect of water on the electrical conductivity of olivine, *Nature,* **443**(7114), 977–980.

Yoshino, T., Matsuzaki, T., Shatskiy, A. & Katsura, T., 2009. The effect of water on the electrical conductivity of olivine aggregates and its implications for the electrical structure of the upper mantle, *Earth planet. Sci. Lett.,* **288**(1), 291–300.

Yoshino, T., Shimojuku, A., Shan, S., Guo, X., Yamazaki, D., Ito, E., Higo, Y. & Funakoshi, K.-I., 2012. Effect of temperature, pressure and iron content on the electrical conductivity of olivine and its high-pressure polymorphs, *J. geophys. Res.: Solid Earth,* **117**(B8), doi:10.1029/2011JB008774.

Zhang, B., Yoshino, T., Xiaoping, W., Matsuzaki, T., Shan, S. & Katsura, T., 2012. Electrical conductivity of enstatite as a function of water content: implications for the electrical structure in the upper mantle, *Earth planet. Sci. Lett.,* **357–358,** 11–20.

Zhang, H., Egbert, G., Chave, A., Huang, Q., Kelbert, A. & Erofeeva, S., 2019. Constraints on the resistivity of the oceanic lithosphere and asthenosphere from seafloor ocean tidal electromagnetic measurements, *Geophys. J. Int.,* **219**(1), 464–478.

Zhao, C. & Yoshino, T., 2016. Electrical conductivity of mantle clinopyroxene as a function of water content and its implication on electrical structure of uppermost mantle, *Earth planet. Sci. Lett.,* **447,** 1–9.

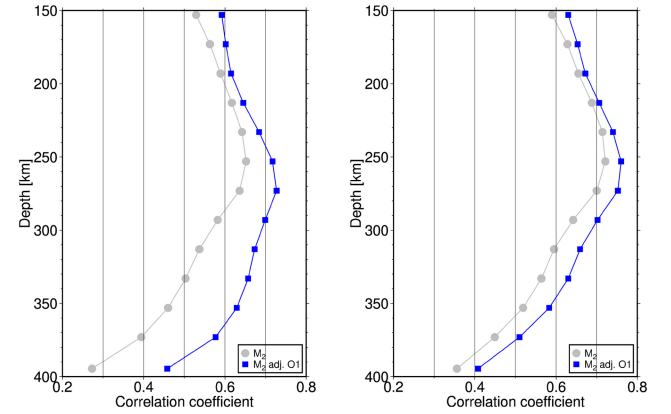## APPENDIX A: SPHERICAL HARMONIC FUNCTIONS

We use the complex SH vectors,

$$S_{jm}^{(-1)}(\Omega) = Y_{jm}(\Omega)e_{\mathrm{r}}, \tag{A1}$$

$$S_{jm}^{(+1)}(\Omega) = \mathrm{grad}_\Omega Y_{jm}(\Omega), \tag{A2}$$

$$S_{jm}^{(0)}(\Omega) = e_{\mathrm{r}} \times \mathrm{grad}_\Omega Y_{jm}(\Omega), \tag{A3}$$

where $Y_{jm}(\Omega)$ is the fully normalized, complex, scalar SH function (Varshalovich *et al.* 1989), e_{r} is the unit vector in the radial direction and grad_Ω is the horizontal gradient operator. The SH

Figure A1. Depth profiles of correlation coefficient beneath the (a) Pacific and (b) Global Ocean in the synthetic test Md60p5j11 of Šachl *et al.* (2022). Grey and blue profiles correspond to the M$_2$ profile and the M$_2$ profile with O$_1$ adjustment, respectively.

vectors $S_{jm}^{(\lambda)}(\Omega)$ obey the orthogonality relation,

$$\int_\Omega \overline{S}_{jm}^{(\lambda)}(\Omega) \cdot S_{j'm'}^{(\lambda')}(\Omega)\, \mathrm{d}\Omega = \delta_{jj'}\delta_{mm'}\delta_{\lambda\lambda'}\left[\delta_{-1\lambda} + \Pi_j\left(1 - \delta_{-1\lambda}\right)\right], \tag{A4}$$

where $\Pi_j = j(j+1)$.

APPENDIX B: O$_1$ TIMF IN THE 3-D INVERSION

Šachl *et al.* (2022) included N$_2$ and O$_1$ periods into the synthetic inversion. However, the conductivity recovered from the joint inversion of M$_2$+N$_2$+O$_1$ TIMFs was not closer to the target conductivity than the M$_2$ solution. We achieved a certain improvement with a modified approach. Instead of running a joint inversion, we first calculate the optimal M$_2$ solution, and then we adjust this solution using O$_1$ TIMF. Besides, we correct the M$_2$ solution only beneath the Pacific Ocean, since the O$_1$ solution was more distant from the target model than the M$_2$ solution in the Atlantic and Indian Oceans, see fig. 8 in Šachl *et al.* (2022). Fig. A1 shows the depth profiles of the correlation coefficient in the Md60p5j11 experiment with noisy data (see Šachl *et al.* 2022, for details). The O$_1$-adjusted profile is closer to the target profile in all inspected depths. The correlation has increased mainly in the layers below the 260 km depth due to the longer period of the O$_1$ tide. The recovered conductivity distributions at 273 and 353 km depths are depicted in Fig. A2. The O$_1$-adjusted solution is close to the M$_2$ solution, but there are many differences in the finer conductivity features.
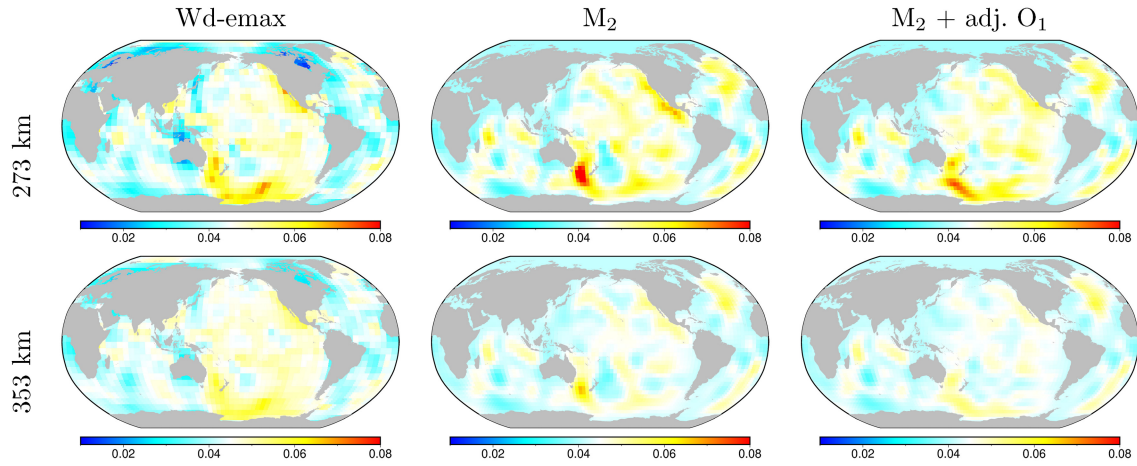
Figure A2. Target Wd-emax model [S m^{-1}] (left-hand column) and the conductivity models [S m^{-1}] recovered from the M$_2$ TIMF (middle column) and M$_2$+O$_1$ TIMFs (right-hand column) in the synthetic test Md60p5j11 of Šachl *et al.* (2022) using the horizontal-smoothness regularization.